molecular pharmaceutics

articles

The Effects of Particle Size and Molecular Targeting on the Intratumoral and Subcellular Distribution of Polymeric Nanoparticles

Helen Lee,[†] Humphrey Fonge,[†] Bryan Hoang,[†] Raymond M. Reilly,[†,‡,§] and Christine Allen*[,†,||,⊥]

Department of Pharmaceutical Sciences, Leslie Dan Faculty of Pharmacy, Division of Nuclear Medicine, University Health Network, Department of Medical Imaging, Faculty of Medicine, and Department of Chemistry, Faculty of Arts and Science, University of Toronto, 144 College Street, Toronto, Ontario, Canada M5S 3M2, and STTARR Innovation Centre, Radiation Medicine Program, Princess Margaret Hospital, University Health Network, Toronto, Ontario, Canada

Received February 16, 2010; Revised Manuscript Received April 26, 2010; Accepted May 17, 2010

Abstract: The current study describes the impact of particle size and/or molecular targeting (epidermal growth factor, EGF) on the *in vivo* transport of block copolymer micelles (BCMs) in athymic mice bearing human breast cancer xenografts that express differential levels of EGF receptors (EGFR). BCMs with diameters of 25 nm (BCM-25) and 60 nm (BCM-60) were labeled with indium-111 (^{111}In) or a fluorescent probe to provide a quantitative and qualitative means of evaluating their whole body, intratumoral, and subcellular distributions. BCM-25 was found to clear rapidly from the plasma compared to BCM-60, leading to an almost 2-fold decrease in their total tumor accumulation. However, the tumoral clearance of BCM-25 was delayed through EGF functionalization, enabling the targeted BCM-25 (T-BCM-25) to achieve a comparable level of total tumor deposition as the nontargeted BCM-60 (NT-BCM-60). Confocal fluorescence microscopy combined with MATLAB analyses revealed that NT-BCM-25 diffuses further away from the blood vessels ($D_{mean} = 42 \pm 9$ μm) following extravasation, compared to NT-BCM-60 which mainly remains in the perivascular regions ($D_{mean} = 23 \pm 4$ μm). The introduction of molecular targeting imposes the "binding site barrier" effect, which retards the tumor penetration of T-BCM-25 ($D_{mean} = 29 \pm 7$ μm, $p < 0.05$). The intrinsic nuclear translocation property of EGF/EGFR leads to a significant increase in the nuclear uptake of T-BCM-25 *in vitro* and *in vivo* via active transport. Overall, these results highlight the need to consider multiple design parameters in the development of nanosystems for delivery of anticancer agents.

Keywords: Copolymer micelles; nanoparticle; in vivo transport; tumor penetration; subcellular distribution; drug delivery

Introduction

In the past two decades, block copolymer micelles (BCMs) have emerged as an important class of nanoparticle-based drug delivery systems (NDDS) for a wide range of therapeutic agents including hydrophobic small molecules,[1−4] radionuclides,[5,6] and genetic materials.[7] In many cases, these

* To whom all correspondence should be addressed. Mailing address: University of Toronto, Department of Pharmaceutical Science, 144 College Street, Toronto, Ontario, Canada M5S 3M2. Phone: (416) 946-8594. Fax: (416) 978-8511. E-mail: cj.allen@utoronto.ca.

† Department of Pharmaceutical Sciences, Leslie Dan Faculty of Pharmacy, University of Toronto.

‡ Division of Nuclear Medicine, University Health Network, University of Toronto.

§ Department of Medical Imaging, Faculty of Medicine, University of Toronto.

|| Department of Chemistry, Faculty of Arts and Science, University of Toronto.

⊥ STTARR Innovation Centre, Radiation Medicine Program, Princess Margaret Hospital, University Health Network.

10.1021/mp100038h © 2010 American Chemical Society
Published on Web 05/17/2010

BCM delivery systems have been designed to retain their cargo until reaching the target site. The performance of the BCMs as NDDS is affected by their physicochemical characteristics including particle size, morphology, thermodynamic and kinetic stability, as well as surface properties (i.e., charge, ligand functionalization, etc.). The extent to which the physicochemical characteristics of BCMs can be altered by manipulating the copolymer composition and/or molecular weight has become well established.[8,9] Meanwhile, only a limited understanding of the relationship between the physicochemical characteristics of BCMs and their biological fate has been obtained to date.

The particle size and surface composition of BCMs have been reported to influence their cellular uptake *in vitro* and whole-body transport *in vivo*. For instance, the functionalization of the BCM surface with targeting ligands has been shown to enhance *in vitro* cellular uptake in cells expressing the corresponding molecular targets.[10,11] Furthermore, the *in vitro* subcellular distribution of BCMs has been qualitatively studied using fluorescence confocal microscopy.[12,13] However, the *in vivo* cellular uptake and subcellular distribution of BCMs as a function of particle size and/or molecular targeting remain virtually unexplored, as studies regarding the *in vivo* fate of BCMs have primarily focused on their whole body clearance and distribution.

It is generally well accepted that particles with diameters of <200 nm tend to have prolonged circulation half-lives and are more favorable for passive targeting to solid tumors via the enhanced permeation and retention (EPR) effect.[14,15] To date, the optimal NDDS particle size for maximizing tumor vascular permeability and tumor penetration remain unknown. Investigative reports indicate that macromolecules (e.g., antibodies, polymer−drug conjugates) of low molecular weight exhibit more rapid plasma and tumoral clearance, but demonstrate enhanced vascular permeability and penetration in solid tumors, compared to their higher molecular weight counterparts.[16−18] Therefore, it is of particular interest to explore whether decreasing the particle size of BCMs can improve their *in vivo* intratumoral transport, while retaining a favorable tumor accumulation profile.

Previously, our group demonstrated that poly(ethylene glycol)-*block*-poly(ε-caprolactone) (PEG-*b*-PCL) BCMs with a mean diameter of 60 nm have limited tumor penetration, leading to low levels of *in vivo* cell uptake at the tumor site in MDA-MB-468 and MCF-7 breast murine tumor models.[19] In addition, molecular targeting was found to delay the tumoral clearance of the BCMs, enhancing their retention in the targeted solid tumors.[19] We speculate that modifying

(1) Matsumura, Y.; Hamaguchi, T.; Ura, T.; Muro, K.; Yamada, Y.; Shimada, Y.; Shirao, K.; Okusaka, T.; Ueno, H.; Ikeda, M.; Watanabe, N. Phase I clinical trial and pharmacokinetic evaluation of NK911, a micelle-encapsulated doxorubicin. *Br. J. Cancer* **2004**, *91*, 1775–1781.

(2) Bae, Y.; Kataoka, K. Intelligent polymeric micelles from functional poly(ethylene glycol)-poly(amino acid) block copolymers. *Adv. Drug Delivery Rev.* **2009**, *61*, 768–84.

(3) Bae, Y.; Nishiyama, N.; Fukushima, S.; Koyama, H.; Yasuhiro, M.; Kataoka, K. Preparation and biological characterization of polymeric micelle drug carriers with intracellular pH-triggered drug release property: tumor permeability, controlled subcellular drug distribution, and enhanced in vivo antitumor efficacy. *Bioconjugate Chem.* **2005**, *16*, 122–30.

(4) Hamaguchi, T.; Matsumura, Y.; Suzuki, M.; Shimizu, K.; Goda, R.; Nakamura, I.; Nakatomi, I.; Yokoyama, M.; Kataoka, K.; Kakizoe, T. NK105, a paclitaxel-incorporating micellar nanoparticle formulation, can extend in vivo antitumour activity and reduce the neurotoxicity of paclitaxel. *Br. J. Cancer* **2005**, *92*, 1240–6.

(5) Fonge, H.; Lee, H.; Reilly, R. M.; Allen, C. Multifunctional Block Copolymer Micelles for the Delivery of ^{111}In to EGFR-Positive Breast Cancer Cells for Targeted Auger Electron Radiotherapy. *Mol. Pharmaceutics* **2010**, *7*, 177–86.

(6) Hruby, M.; Konak, C.; Kucka, J.; Vetrik, M.; Filippov, S. K.; Vetvicka, D.; Mackova, H.; Karlsson, G.; Edwards, K.; Rihova, B.; Ulbrich, K. Thermoresponsive, hydrolytically degradable polymer micelles intended for radionuclide delivery. *Macromol. Biosci.* **2009**, *9*, 1016–27.

(7) Nishiyama, N.; Kataoka, K. Current state, achievements, and future prospects of polymeric micelles as nanocarriers for drug and gene delivery. *Pharmacol. Ther.* **2006**, *112*, 630–48.

(8) Allen, C.; Maysinger, D.; Eisenberg, A. Nano-engineering block copolymer aggregates for drug delivery. *Colloids Surf., B* **1999**, *16*, 3–27.

(9) Srinivas, G.; Discher, D. E.; Klein, M. L. Self-assembly and properties of diblock copolymers by coarse-grain molecular dynamics. *Nat. Mater.* **2004**, *3*, 638–44.

(10) Zeng, F.; Lee, H.; Allen, C. Epidermal growth factor-conjugated poly(ethylene glycol)-block- poly(delta-valerolactone) copolymer micelles for targeted delivery of chemotherapeutics. *Bioconjugate Chem.* **2006**, *17*, 399–409.

(11) Prabaharan, M.; Grailer, J. J.; Pilla, S.; Steeber, D. A.; Gong, S. Folate-conjugated amphiphilic hyperbranched block copolymers based on Boltorn H40, poly(L-lactide) and poly(ethylene glycol) for tumor-targeted drug delivery. *Biomaterials* **2009**, *30*, 3009–19.

(12) Maysinger, D.; Lovric, J.; Eisenberg, A.; Savic, R. Fate of micelles and quantum dots in cells. *Eur. J. Pharm. Biopharm.* **2007**, *65*, 270–81.

(13) Savic, R.; Luo, L.; Eisenberg, A.; Maysinger, D. Micellar nanocontainers distribute to defined cytoplasmic organelles. *Science* **2003**, *300*, 615–8.

(14) Alexis, F.; Pridgen, E.; Molnar, L. K.; Farokhzad, O. C. Factors affecting the clearance and biodistribution of polymeric nanoparticles. *Mol. Pharmaceutics* **2008**, *5*, 505–15.

(15) Mikhail, A. S.; Allen, C. Block copolymer micelles for delivery of cancer therapy: transport at the whole body, tissue and cellular levels. *J. Controlled Release* **2009**, *138*, 214–23.

(16) Dreher, M. R.; Liu, W.; Michelich, C. R.; Dewhirst, M. W.; Yuan, F.; Chilkoti, A. Tumor vascular permeability, accumulation, and penetration of macromolecular drug carriers. *J. Natl. Cancer Inst.* **2006**, *98*, 335–44.

(17) Thurber, G. M.; Schmidt, M. M.; Wittrup, K. D. Antibody tumor penetration: transport opposed by systemic and antigen-mediated clearance. *Adv. Drug Delivery Rev.* **2008**, *60*, 1421–34.

(18) Yokota, T.; Milenic, D. E.; Whitlow, M.; Schlom, J. Rapid tumor penetration of a single-chain Fv and comparison with other immunoglobulin forms. *Cancer Res.* **1992**, *52*, 3402–8.

(19) Lee, H.; Hoang, B.; Fonge, H.; Reilly, R. M.; Allen, C. In vivo Distribution of Polymeric Nanoparticles at the Whole Body, Tumor, and Cellular Levels. *Pharm. Res.* **2010**, E-pub ahead of print, DOI, 10.1007/s11095-010-0068-z.

the BCM size and/or conjugating a targeting ligand to the BCM surface can potentially alter their whole-body and tumoral clearance, cellular uptake, as well as subcellular distribution. Therefore, the goal of the current study is to evaluate the effects of particle size and/or molecular targeting on the *in vivo* transport of BCMs at the whole body, tissue, and cellular levels in tumor-bearing mice. By modifying the molecular weights of both the PEG and the PCL blocks of the copolymer, BCMs with diameters of 25 and 60 nm were prepared. The BCM surface was also functionalized with epidermal growth factor (EGF), which is known to facilitate nuclear translocation when bound to its molecular target, the EGF receptor (EGFR).[20,21] In addition, BCMs were labeled with indium-111 (^{111}In) or Alexa Fluor 647 (AF647; λ_{ex} = 650 nm, λ_{em} = 665 nm) as tracers, which can be detected by γ-counting or confocal fluorescence microscopy, respectively. The whole body transport of BCMs as a function of particle size and/or molecular targeting was examined by traditional pharmacokinetics and biodistribution studies. Image-based analyses including autoradiography and confocal florescence microscopy were used to map the intratumoral distribution of BCMs with respect to tumor neovasculature at submm spatial resolution. Finally, the tumors were fractionated in order to quantify the amount of BCMs localizing in the extracellular, cytoplasmic, and nuclear compartments *in vitro* and *in vivo*. Overall findings from these studies provide invaluable insight into the influence of BCM size and molecular targeting on the fate of these NDDS *in vivo*.

Experimental Section

Materials. Methoxy poly(ethylene glycol) of different molecular weights (MePEG; M_n = 5000, M_w/M_n = 1.06; M_n = 2000, M_w/M_n = 1.06) were purchased from Polymer Source Inc. (Montreal, QC, Canada) and Sigma-Aldrich (Oakville, ON, Canada). Heterobifunctional α-hydroxy-ω-amino poly(ethylene glycol) (HO-PEG-NH_2; M_n = 5000, M_w/M_n = 1.08; M_n = 2000, M_w/M_n = 1.04) and α-hydroxy-ω-carboxyl poly(ethylene glycol) (HO-PEG-COOH, M_n = 4910, M_w/M_n = 1.05) were purchased from Jenkem Technology Inc. (Beijing, China). Human EGF, N-hydroxy succinimide (NHS), *N*,*N*-dimethylformamide (DMF), *N*,*N*′-dicyclohexyl carbodiimide (DCC), silica gel 100 C_8-reversed phase column, dimethyl sulfoxide (DMSO), and triethylamine (TEA) were purchased from Sigma-Aldrich (Oakville, ON, Canada). Alexa Fluor 647 (AF647) carboxylic acid succinimidyl ester was purchased from Molecular Probes (Eugene, OR). ^{111}In-chloride was obtained from MDS Nordion (Kanata, ON, Canada). 2-(4-Isothiocyanatobenzyl)diethylenetriaminepentaacetic acid (*p*-SCN-Bn-DTPA) was purchased from Macrocyclics Inc. (Dallas, TX). Toluene, dichloromethane, and ε-caprolactone (ε-CL) were purchased from Sigma-Aldrich (Oakville, ON, Canada), dried under calcium hydride and distilled prior to use. All chemicals were used as received unless otherwise specified.

Synthesis, Purification, and Characterization of Copolymers. MePEG-*b*-PCL, NH_2-PEG-*b*-PCL, and COOH-PEG-*b*-PCL copolymers were synthesized via metal-free cationic ring-opening polymerization of ε-CL using established methods described in detail elsewhere.[22,23] Characterization including ^{1}H NMR assignments of $MePEG_{5000}$-*b*-PCL_{5000}, $MePEG_{2000}$-*b*-PCL_{2000}, COOH-PEG_{5000}-*b*-PCL_{5000}, COOH-PEG_{2000}-*b*-PCL_{2000} and NH_2-PEG_{5000}-*b*-PCL_{5000} were published in previous reports.[19,22,24] The ^{1}H NMR assignments for NH_2-PEG_{2000}-*b*-PCL_{2000} copolymer are as follows: δ = 1.39 ppm (2H, CO−CH_2−CH_2−CH_2−CH_2−CH_2−O), 1.61 ppm (4H, CO−CH_2−CH_2−CH_2−CH_2−CH_2−O), 1.98 ppm (2H, NH_2−CH_2−CH_2), 2.29 ppm (2H, CO−CH_2−CH_2−CH_2−CH_2−CH_2−O), 3.61 ppm (4H, −O−CH_2−CH_2), 3.69 ppm (2H, CH_2−CH_2−OH), 4.06 ppm (2H, CO−CH_2−CH_2−CH_2−CH_2−CH_2-O), and 4.21 ppm (2H, O−CH_2−CH_2-O−CO). NHS-PEG-*b*-PCL copolymer activated from COOH-PEG-*b*-PCL copolymer in the presence of NHS and DCC were used for preparation of EGF-PEG-*b*-PCL via an established method as described elsewhere.[19,24] Thermal analysis of the MePEG-*b*-PCL copolymers was performed by differential scanning calorimetry using a DSC Q100 (TA Instruments Inc.; New Castle, DE) under nitrogen at a heating rate of 5 °C/min.[25]

For radiolabeling of copolymer, DTPA-PEG-*b*-PCL copolymer was prepared by conjugating 2× molar excess of *p*-SCN-Bn-DTPA with NH_2-PEG-*b*-PCL.[22] The final product is purified using a size-exclusion column (Bio-Gel P2; BioRad, CA), lyophilized in aliquots, and stored at −20 °C. Immediately before the experiments, purified DTPA-PEG-*b*-PCL copolymer was incubated with ^{111}In for 30 min in 0.1 M sodium acetate buffer (pH = 6). The radiochemical purity of the copolymer was determined to be ≥94% by instant layer chromatography (ITLC), which was developed in 0.1 M sodium citrate buffer (pH = 6).

(20) Holt, S. J.; Alexander, P.; Inman, C. B.; Davies, D. E. Epidermal growth factor induced tyrosine phosphorylation of nuclear proteins associated with translocation of epidermal growth factor receptor into the nucleus. *Biochem. Pharmacol.* **1994**, *47*, 117–26.

(21) Hu, M.; Scollard, D.; Chan, C.; Chen, P.; Vallis, K.; Reilly, R. M. Effect of the EGFR density of breast cancer cells on nuclear importation, in vitro cytotoxicity, and tumor and normal-tissue uptake of [^{111}In]DTPA-hEGF. *Nucl. Med. Biol.* **2007**, *34*, 887–96.

(22) Hoang, B.; Lee, H.; Reilly, R. M.; Allen, C. Non-Invasive Monitoring of the Fate of ^{111}In-Labeled Block Copolymer Micelles by High Resolution and High Sensitivity MicroSPECT/CT Imaging. *Mol. Pharmaceutics* **2009**, *6*, 581–92.

(23) Zeng, F.; Allen, C. Synthesis of carboxy-functionalized heterobifunctional poly(ethylene glycol) by a thiol-anionic polymerization method. *Macromolecules* **2006**, *39*, 6391–6398.

(24) Lee, H.; Hu, M.; Reilly, R. M.; Allen, C. Apoptotic epidermal growth factor (EGF)-conjugated block copolymer micelles as a nanotechnology platform for targeted combination therapy. *Mol. Pharmaceutics* **2007**, *4*, 769–81.

(25) Lee, H.; Zeng, F.; Dunne, M.; Allen, C. Methoxy poly(ethylene glycol)-block-poly(delta-valerolactone) copolymer micelles for formulation of hydrophobic drugs. *Biomacromolecules* **2005**, *6*, 3119–28.

For preparation of fluorescently labeled copolymer, AF647 carboxylic acid succinimidyl ester (4× molar excess) was conjugated to NH_2-PEG-*b*-PCL in DMSO with TEA (30× molar excess of NH_2 group) for 24 h at room temperature. AF647-PEG-*b*-PCL was purified using a silica gel 100 C_8-reversed phase column (Sigma-Aldrich, Oakville) packed in 50/50 acetonitrile/water. The column was equilibrated with water for 3 h prior to injection of the reaction mixture. Free AF647 was eluted with a 3-bed volume of water, followed by a 2-bed volume of a 90/10 acetonitrile/water mixture for elution of the AF647-PEG-*b*-PCL conjugate. The purity of the conjugate was confirmed using high performance liquid chromatography (HPLC) equipped with a fluorescence detector (Agilent Technologies Inc., CA) and a Styragel HR2 column (effective molecular-weight range of 500 to 20,000; Waters, MA). Filtered HPLC grade DMF was used as the mobile phase, and the AF647 signal was detected at λ_{ex} = 650 nm and λ_{em} = 665 nm. Complete separation of unconjugated AF647 and AF647-PEG-*b*-PCL was achieved with a flow rate of 0.1 mL/min.

Preparation and Characterization of ^{111}In-Labeled and AF647-Labeled BCMs. BCMs were prepared as previously described using the dry-down method.[19] Briefly, MePEG-*b*-PCL copolymer dissolved in DMF was dried under nitrogen to form a copolymer film, and subsequently hydrated with phosphate-buffered saline (PBS) (pH = 7.4, 0.01 M) at 60 °C to form nontargeted-BCMs (NT-BCMs, EGF−) at a concentration of 5 mM. ^{111}In-PEG-*b*-PCL (<1 mol %), AF647-PEG-*b*-PCL (0.8 mol %), or EGF-PEG-*b*-PCL copolymers (0.2 mol %) were incorporated into the preformed NT-BCMs via the transfer method, to form ^{111}In-labeled BCMs, AF647-labeled BCMs, or targeted-BCMs (T-BCMs, EGF+), respectively.[19,24] The dissociation of ^{111}In from the BCMs and the transchelation of ^{111}In to transferrin under physiological conditions were found to be minimal as published in detail elsewhere.[22]

The zeta potential and particle size of BCMs were determined using the 90 Plus Particle Size Analyzer (Brookhaven Instruments Corp., NY). Nonradioactive BCM samples (chelated with $InCl_3$) were diluted to a concentration of 1 mg/mL immediately prior to measurements.

Tumor Inoculation. Animal studies were conducted under a protocol approved by the Animal Care Committee at the University Health Network (AUP 989.3). Balb/C female athymic mice of 4−6 weeks of age (16−20 g) were used for tumor inoculation.[19] For the EGFR-overexpressing tumor model, 10×10^6 MDA-MB-468 cells (10^6 EGFR/cell) suspended in DMEM supplemented with 10% FBS and 1% penicillin−streptomycin were injected subcutaneously into the right flank. Mice bearing MCF-7 tumor (10^4 EGFR/cell) represent the xenograft tumor model expressing low level of EGFR. The MCF-7 tumor-bearing mice were implanted intradermally with a 17-β-estradiol pellet (Innovative Research of America) prior to subcutaneous injection of 20×10^6 MCF-7 cells.

Pharmacokinetics and Biodistribution Studies. At two to three weeks postinoculation, tumor-bearing mice (i.e., tumor diameters of 4−8 mm) were injected with ^{111}In-BCMs intravenously at a dose of 25 μmol copolymer/kg (3−4 MBq/mouse). Blood samples were collected from the saphenous vein at 5 min, 15 min, 30 min, 1, 2, 4, 8, 12, 24, and 48 h postinjection (hpi). At the terminal time-point of 48 hpi, tissue samples including the heart, lung, liver, spleen, kidneys, and tumor were harvested for γ-counting in order to determine the amount of ^{111}In-BCMs in each organ.

Autoradiography. Autoradiographic imaging was used as a tool for mapping the intratumoral distribution of ^{111}In-BCMs with respect to tumor neovasculature, following previously reported procedures.[19] Briefly, excised tumors embedded in Tissue-Tek OCT compound were frozen in liquid nitrogen, and were cut into 8 μm thick tissue sections. The intratumoral distribution of ^{111}In-BCMs within the tumor section was recorded using the Cyclone Plus Storage Phosphor System (PerkinElmer Inc., MA). For visualization of tumor blood vessels, the consecutive tumor section was stained with anti-CD-31 antibody (Pathology Research Program, University Health Network).

A region of interest (ROI) grid composed of 0.5 × 0.5 mm squares was arbitrarily assigned to each autoradiographic image. The amount of ^{111}In-BCMs in each square was quantified using the OptiQuant Image Analysis Software (PerkinElmer Inc., MA) and was expressed as digital light units (DLU). The same ROI grid was then coregistered onto the corresponding CD-31-stained tumor section. The total area of blood vessels (measured in pixels) in each 0.5 × 0.5 mm square was determined by a customized program written in MATLAB (version 7.5.0.342, R2007b). Colocalization of ^{111}In-BCMs and blood vessels were then quantified using Pearson correlation and linear regression analyses.

Confocal Fluorescence Microscopy. MDA-MB-468 tumor-bearing mice were injected intravenously with AF647-BCMs at a dose of 25 μmol copolymer/kg (4 nmol AF647 equivalent). At 48 hpi, each mouse was sacrificed by cervical dislocation and the tumor was excised. The tumor was then frozen and cut into 8 μm thick sections as described above. Tumor sections were stained with FITC-CD31-antibody and DAPI (Pathology Research Program, University Health Network) for visualization of blood vessels and cell nuclei, respectively. The tumor sections were then viewed under an inverted microscope (Zeiss LSM510 META NLO) equipped with both confocal and two-photon scanning systems. FITC-CD31-antibody (λ_{ex} = 488 nm and λ_{em} = 515 nm) and AF647-BCMs (λ_{ex} = 650 nm and λ_{em} = 665 nm) were excited by the argon (488 nm) and the HeNe (633 nm) lasers, respectively. DAPI (λ_{ex} = 350 nm and λ_{em} = 452 nm) was excited by the tunable two-photon Chameleon laser at 750 nm. Images were obtained using a FLUAR 20x/0.75 NA lens.

Semiquantitative analysis of BCM tumor penetration was carried out using a reported method with modifications.[26] Prior to analyses, confocal fluorescence images underwent

(26) Primeau, A. J.; Rendon, A.; Hedley, D.; Lilge, L.; Tannock, I. F. The distribution of the anticancer drug Doxorubicin in relation to blood vessels in solid tumors. *Clin. Cancer Res.* **2005**, *11*, 8782–8.

noise reduction to remove speckles using ImageJ (version 1.38x, NIH). CD-31-stained images were then converted to binary images with objects smaller than 5 μm removed. Images consisting of only the AF647 signals were converted to 8-bit gray scale images. The Euclidian distance between each AF647-positive pixel (BCMs) and the nearest CD-31-positive pixel (blood vessels) were computed using a customized algorithm written in MATLAB. A histogram (percentage of total AF647-intensity per image vs distance from nearest blood vessel) is produced for each tumor section image. Tumor penetration of BCMs was evaluated by analyzing at least four tumor section images for each treatment group.

***In Vivo* Subcellular Fractionation.** Tumors were fractionated following protocols optimized in our laboratory that were modified from manufacturer's procedures (Nuclei PURE Prep Nuclei Isolation Kit; Sigma-Aldrich, Oakville).[21,27] Briefly, tumor samples collected at 48 hpi were minced with a scalpel and were transferred to a tube containing sodium acetate buffer (0.2 M, pH 2.5). The tissues were disaggregated using a sonic dismembrator, model 100 (Fisher Scientific, Pittsburgh, PA). 2.2 mL of the acetate buffer was added to the homogenized samples followed by 10 min incubation on ice. Extracellular and membrane bound radioactivity (supernatant) were separated from the cells after centrifugation at 6311*g* for 10 min, followed by two PBS rinses. Subsequently, cells were lysed by homogenizing for 45 s in 2.5 mL of cell lysis solution (11 mL Nuclei PURE lysis buffer, 11 μL of 1 M dithiothreitol (DTT), and 110 μL of 10% Triton X-100). The purified nuclei were obtained by ultracentrifugation through a sucrose cushion solution (27 mL of 2 M Nuclei PURE sucrose cushion solution, 3 mL of Nuclei PURE sucrose cushion buffer, and 30 μL of 1 M DTT). Briefly, the lysate mixed with the sucrose cushion solution was transferred to a 15 mL of NALGENE high-speed centrifugation tube (Nalge Nunc International; Rochester, NY). The samples were then centrifuged at 20200*g* using a Sorvall RC-6 ultracentrifuge (Mandel Scientific Company Inc.; Guelph, ON, Canada). The supernatant (cytoplasm) was separated from the nuclei, and the amount of ^{111}In-BCMs in the three fractions was measured by γ-counting. This method was validated previously and was shown to result in highly pure cytoplasmic fractions.[21,27] Homogenization of the tissue samples likely leads to a certain degree of cell rupture; therefore the amount of ^{111}In-BCMs measured in the intracellular fractions may be an underestimate. However, it should be noted that all tumors harvested from each treatment group were disaggregated in the same manner. In this way, the data afforded a relative comparison among treatment groups with no preferential bias toward mice treated with NT-BCM-25, T-BCM-25, NT-BCM-60, or T-BCM-60.

***In Vitro* Subcellular Fractionation.** *In vitro* subcellular fractionation studies were performed following the manufacturer's protocol (Nuclei EZ Prep Nuclei Isolation Kit; Sigma-Aldrich, Oakville) with slight modification.[21] Briefly, MDA-MB-468 (10^6 EGFR/cell) or MCF-7 (10^4 EGFR/cell) breast cancer cells were added to a 100 mm cell culture dish at a cell density of 2,000,000 cells/dish and were incubated for 24 h to allow for growth recovery. The growth medium was then removed and replaced with 10 mL of fresh medium containing ^{111}In-DTPA (negative control), ^{111}In-EGF (positive control), or ^{111}In-BCMs (NT- and T-BCMs, ~100 kBq/mL). Following a 24 h incubation period, cells were washed with acidic PBS (pH = 2.5, 0.01 M) to remove membrane bound ^{111}In molecules (i.e., membrane fraction). The cells were then collected using a cell scraper in the presence of Nuclei EZ lysis buffer. The cell suspension was vortexed and incubated on ice for 10 min. The cells were then centrifuged for 5 min at 3000*g* and 4 °C; the supernatant collected contains the cytoplasmic fraction. The cells were then resuspended again in Nuclei EZ lysis buffer, and the above procedure was repeated to collect the remaining cytoplasmic fraction. The final pellet containing intact cell nuclei was resuspended in PBS. Each subcellular fraction was then counted using the γ-counter to determine the amount of ^{111}In molecules within each fraction.

Statistical Analyses. All results were obtained from data groups of $n \geq 3$ and were expressed as mean $\pm$ standard deviation (SD). Statistical analyses were performed using SPSS (Statistical Package for the Social Sciences, version 14.0). The two-sample *t* test was used to measure statistical significance between pairs of results, and $P < 0.05$ was considered to be significant. For statistical analyses among three or more groups, one-way analysis of variance (ANOVA) was used and subsequent multiple comparisons with Bonferroni correction were performed if any statistical significance was detected by the ANOVA *F*-test. Pearson correlation and linear regression analysis were used for analyzing data from the autoradiography studies.

Results

Physicochemical Characterization of Copolymers and BCMs. Table 1 summarizes the physicochemical properties of the BCMs and their copolymer compositions. BCMs formed from PEG_{2000}-*b*-PCL_{2000} or PEG_{5000}-*b*-PCL_{5000} had mean effective diameters of 26.4 $\pm$ 0.7 nm (NT-BCM-25) or 57.4 $\pm$ 8 nm (NT-BCM-60), respectively. Although the hydrodynamic diameter of EGF is reported to be approximately 4 nm,[28] functionalization of the BCM surface with EGF did not alter the particle size significantly ($p > 0.5$). These results were in agreement with our previously published report regarding the characterization of the BCM-25 system.[24] In addition, the BCMs have been shown to remain stable under physiologically relevant conditions

(27) Costantini, D. L.; Chan, C.; Cai, Z.; Vallis, K. A.; Reilly, R. M. (111)In-labeled trastuzumab (Herceptin) modified with nuclear localization sequences (NLS): an Auger electron-emitting radiotherapeutic agent for HER2/neu-amplified breast cancer. *J. Nucl. Med.* **2007**, *48*, 1357–68.

(28) Thorne, R. G.; Hrabetova, S.; Nicholson, C. Diffusion of epidermal growth factor in rat brain extracellular space measured by integrative optical imaging. *J. Neurophysiol.* **2004**, *92*, 3471–81.

Table 1. Physicochemical Properties of PEG-*b*-PCL Copolymers and BCMs

copolymer	PEG_{2000}-*b*-PCL_{2000}	PEG_{5000}-*b*-PCL_{5000}
PEG block $M_{n,NMR}$	2000	5000
PCL block $M_{n,NMR}$	1900	4700
copolymer T_m (°C)	45.0	55.4
copolymer T_g (°C)	−44.6	−30.7
CMC[a] (M)	3.6×10^{-6}	3.8×10^{-6}

	PEG_{2000}-*b*-PCL_{2000}		PEG_{5000}-*b*-PCL_{5000}	
	NT-BCM-25	T-BCM-25	NT-BCM-60	T-BCM-60
mean diameter[b] (nm)	26.4 ± 0.7	26.2 ± 0.4	57.4 ± 8	60.9 ± 0.7
zeta potential[b] (mV)	−5.2	−5.1	−6.4	−7.3

[a] CMC = critical micelle concentration (as previously determined).[22] [b] Mean diameter and zeta potential of NT-BCM-60 and T-BCM-60 published previously ($n = 3$, mean ± SD).[19]

following incubation in 45 g/L bovine serum albumin at 37 °C for a one week period.[22] All BCMs were found to have similar zeta potentials, which infers that particle charge does not have a profound effect on the behavior of these systems in the current study. The thermodynamic stability of the BCMs, as denoted by the critical micelle concentrations (CMC) of the copolymers (PEG_{2000}-*b*-PCL_{2000} and PEG_{5000}-*b*-PCL_{5000}), were also found to be comparable (3.6 μM vs 3.8 μM).

Pharmacokinetics of BCM-25 and BCM-60 in MDA-MB-468 Tumor-Bearing Mice. Figure 1 and Table 2 present the pharmacokinetics profiles and parameters of MDA-MB-468 tumor-bearing mice injected with BCM-25 or BCM-60 (NT-BCMs and T-BCMs). Overall, conjugation of EGF to the BCM surface did not affect the pharmacokinetics of BCMs in the EGFR-overexpressing tumor-bearing mice (10^6 EGFR/cell) ($p > 0.503$). Our previous study revealed similar findings for BCM-60 (+/−EGF) in mice bearing breast cancer xenografts expressing low levels of EGFR (MCF-7, 10^4 EGFR/cell).[19] In contrast, particle size was shown to have a tremendous impact on the plasma clearance of BCMs in the current study. For instance, BCM-25 (NT-BCMs and T-BCMs) exhibited much shorter circulation half-lives than BCM-60 (2.2-fold decrease in $t_{1/2,\beta}$). The total clearance (CL_{total}) and volume of distribution at steady state (V_{dss}) of NT-BCMs increased from 0.06 ± 0.02 mL/h to 1.07 ± 0.08 mL/h ($p < 0.001$) and 2.0 ± 0.1 mL to 14.6 ± 0.8 mL ($p < 0.001$), respectively, as the mean particle size was decreased from 60 to 25 nm.

Table 2. Summary of Pharmacokinetics Parameters for BCM-25 and BCM-60 Obtained Using 2-Compartmental Analyses for Curve Fitting ($n \geq 4$, Mean ± SD)

	MDA-MB-468 xenograft			
parameters	NT-BCM-25	T-BCM-25	NT-BCM-60[a]	T-BCM-60[a]
$t_{1/2,\alpha}$ (h)	0.71 ± 0.4	1.04 ± 0.5	0.42 ± 0.2	0.35 ± 0.2
$t_{1/2,\beta}$ (h)	13 ± 1	13 ± 2	29 ± 4	30 ± 3
V_1 (mL)	3.3 ± 0.9	3.7 ± 2	1.3 ± 0.3	1.4 ± 0.2
V_{dss} (mL)	14.6 ± 0.8	13.0 ± 3	2.0 ± 0.1	2.08 ± 0.09
CL_{total} (mL/h)	1.07 ± 0.08	1.11 ± 0.3	0.06 ± 0.02	0.05 ± 0.01
AUC_{total} (% i.d.·h/L)	95 ± 6	95 ± 20	2030 ± 400	1900 ± 200

[a] Data for BCM-60 is referenced from a previous report.[19]

Biodistribution and Total Tumor Accumulation of BCM-25 and BCM-60. Figures 2a and 2b present the biodistribution of BCMs (NT-BCM-25, T-BCM-25, NT-BCM-60, T-BCM-60) in MDA-MB-468 and MCF-7 tumor-bearing mice, respectively. At 48 hpi, no statistical difference was detected in the accumulation of BCMs in organs responsible for clearance (liver, spleen, kidneys) among all the treatment groups ($p > 0.260$). The effect of molecular targeting on the tumor accumulation of BCMs was only observed in mice expressing high levels of EGFR (MDA-MB-468, Figure 2a), where the tumor uptake of T-BCM-25 and T-BCM-60 was found to be 2.1- ($p = 0.002$) and 1.3-fold ($p = 0.022$) higher, respectively, than that of their nontargeted counterparts.

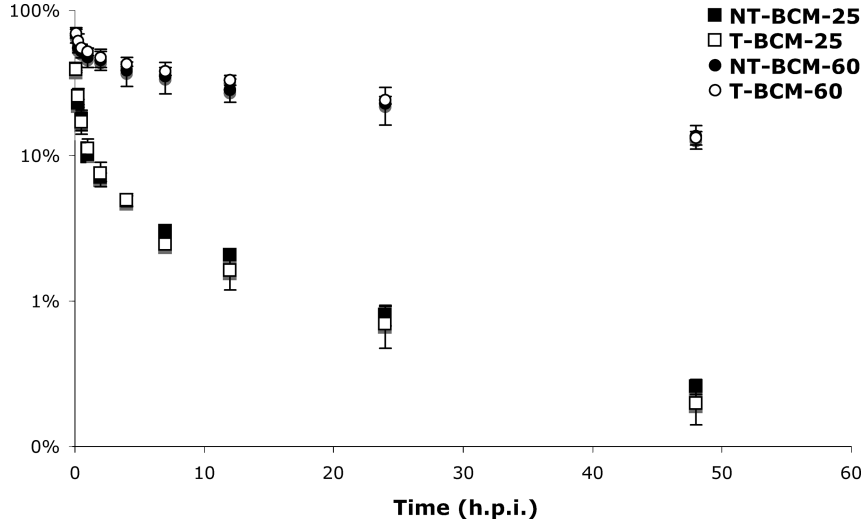

Figure 1. Pharmacokinetics profiles of ^{111}In-labeled NT-BCM-25, T-BCM-25, NT-BCM-60, and T-BCM-60 in MDA-MB-468 tumor bearing mice administered at a dose of 25 μmol of copolymer/kg ($n \geq 4$, error bars represent SD). Data for NT-BCM-60 and T-BCM-60 is referenced from a study previously published by our group[19] ($n \geq 4$, error bars represent SD).

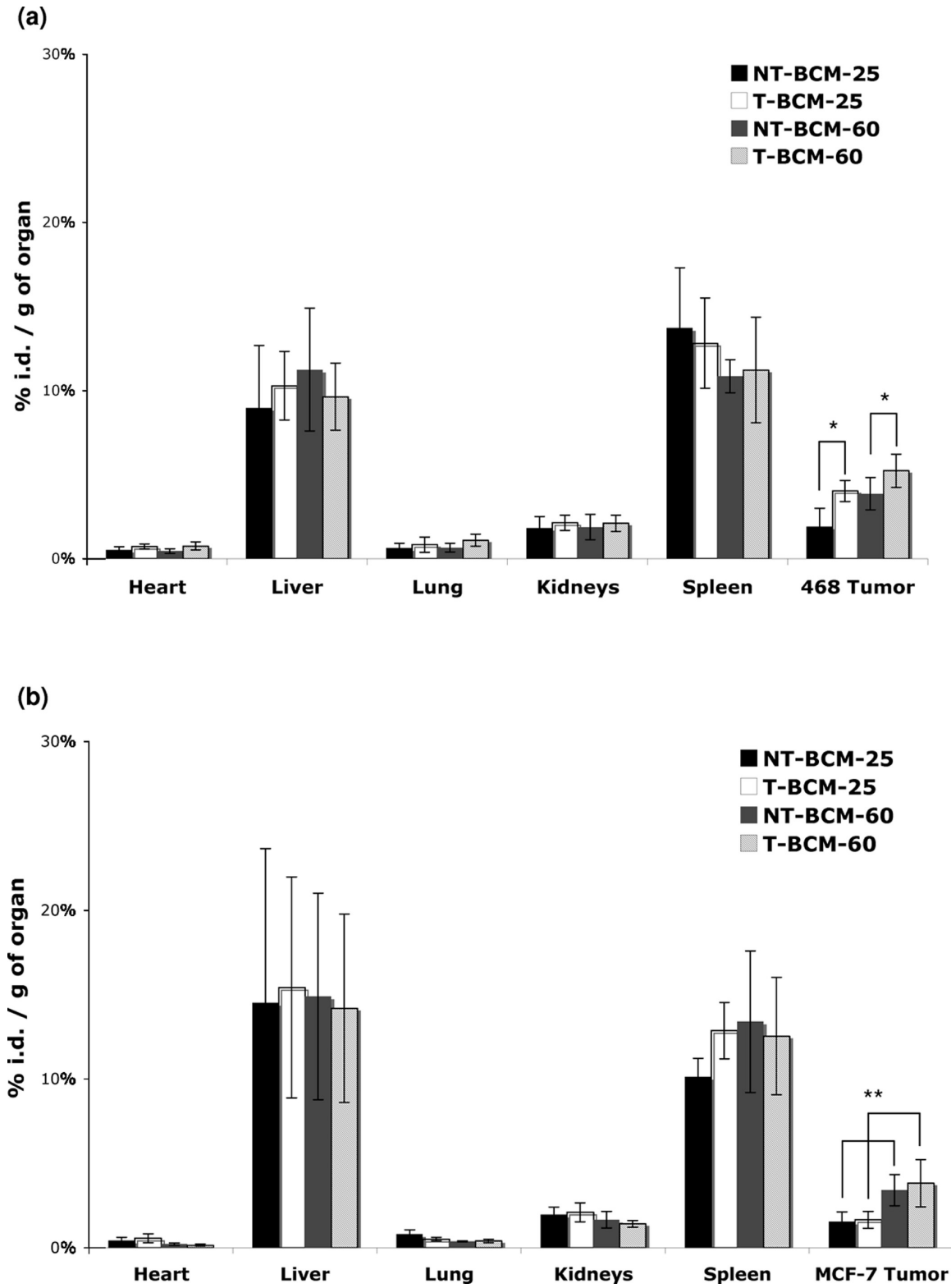

Figure 2. Biodistribution and total tumor accumulation of ^{111}In-labeled NT-BCM-25, T-BCM-25, NT-BCM-60, and T-BCM-60 injected at a dose of 25 μmol copolymer/kg in (a) MDA-MB-468 and (b) MCF-7 tumor-bearing mice ($n \geq 3$, error bars represent SD). Data for NT-BCM-60 and T-BCM-60 are referenced from a study previously published by our group.[19] *$p < 0.022$ for comparison between NT-BCMs and T-BCMs as determined by independent t test. **$p < 0.001$ for comparison between BCM-25 and BCM-60 as determined by independent t test.

On the other hand, a reduction in the particle size of BCMs consistently led to lower tumor deposition in both tumor models. For instance, the MDA-MB-468 tumor uptake of NT-BCM-25 was 2.0-fold lower than that of the NT-BCM-

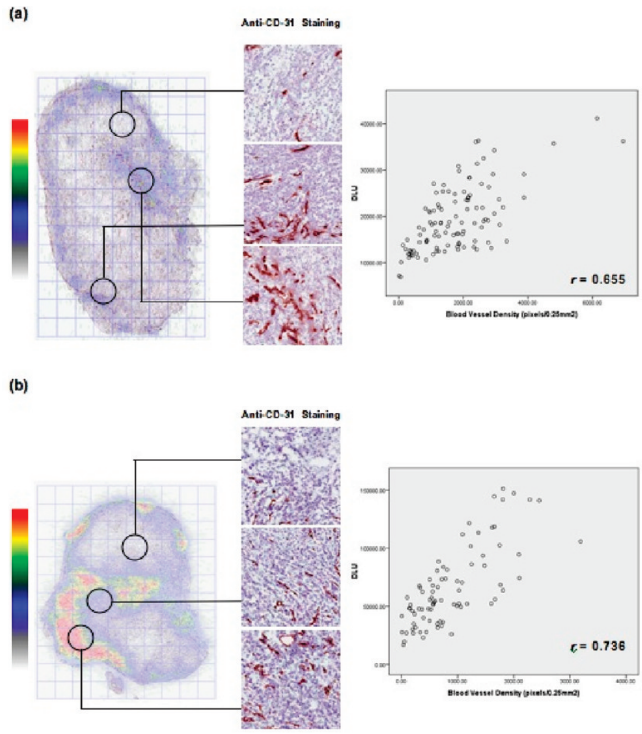

Figure 3. Intratumoral distribution of ^{111}In-labeled (a) NT-BCM-25 and (b) T-BCM-25 at 48 hpi in MDA-MB-468 tumors captured by autoradiography. 8 μm thick tumor sections were imaged using a Cyclone Plus Storage Phosphor System. Consecutive tumor sections were stained with anti-CD-31-antibody for visualization of tumor endothelial cells (blood vessels stained in brown). Correlation analyses of tumor vessel densities and BCM localization within an arbitrarily assigned ROI grid (consisting of 0.5 $\times$ 0.5 mm areas) are shown on the right.

60 ($p = 0.004$). Also, the accumulation of NT-BCM-25 and T-BCM-25 in the MCF-7 tumors was 1.7- and 1.8-fold lower than that of NT-BCM-60 and T-BCM-60 ($p < 0.003$), respectively.

Autoradiography: Intratumoral Distribution of BCM-25 and BCM-60. Figure 3 includes representative autoradiographic images obtained at 48 hpi from MDA-MB-468 tumor-bearing mice injected with ^{111}In-BCM-25 (NT-BCMs and T-BCMs). It can be seen that the intratumoral distribution of BCM-25 is highly heterogeneous, with regions of low blood vessel densities showing a lack of BCM localization. Examples of analyses of the correlation between tumor blood vessel densities and BCM-25 localization are shown on the right sides of Figures 3a and 3b. The mean correlation coefficients ($n \geq 4$) for NT-BCM-25 and T-BCM-25 were found to be 0.70 $\pm$ 0.2 and 0.70 $\pm$ 0.2 for the MDA-MB-468 tumors and 0.70 $\pm$ 0.1 and 0.65 $\pm$ 0.07 for the MCF-7 tumors, respectively. These results were statistically similar ($p = 0.983$) to results obtained in mice injected with BCM-60 (data not shown here[19]), indicating that no significant difference in the intratumoral distribution of BCM-25 and BCM-60 was detected at the millimeter scale (ROI = 0.5 $\times$ 0.5 mm). However, it should be noted that scattering of radioactivity leads to reduced spatial resolution and prohibits its application in imaging BCM distribution at the microscopic level. In order to better evaluate whether particle size and/or molecular targeting affects the tumor penetration of BCMs, confocal fluorescence microscopy was exploited for image-based analysis at the micrometer scale.

Confocal Fluorescence Microscopy: Tumor Penetration of BCM-25 and BCM-60. Figures 4a to 4d show several representative confocal fluorescence images obtained from MDA-MB-468 tumor-bearing mice injected with AF647-BCMs (4 nmol AF647 equivalent). The red, blue, and green signals represent fluorescence signals corresponding to the AF647-BCMs, cell nuclei (DAPI), and the outline of blood vessels (FITC-anti-CD-31-antibody), respectively. An overlay image of the above signals was also included (third image from the left). It can be seen that BCM-60 (NT- and T-BCM) mainly reside in close proximity to the blood vessels (Figures 4c and 4d), while BCM-25 seem to have a much more homogeneous distribution throughout the imaged regions even when the blood vessels were segregated (Figures 4a and 4b).

Examples of quantitative analyses of BCM tumor penetration within the images presented in Figures 4a to 4d are shown in the right panel of Figure 4. It is clearly demonstrated that the distribution of BCM-25 was much broader than that of BCM-60. Comprehensive analyses of multiple tumor sections for each treatment group revealed that the mean localization distances of NT-BCM-25, T-BCM-25, NT-BCM-60, and T-BCM-60 with respect to the nearest blood vessels were 42 $\pm$ 9 μm, 29 $\pm$ 7 μm, 23 $\pm$ 4 μm, and 21 $\pm$ 9 μm, respectively. Significant differences in the tumor penetration of BCMs were observed between NT-BCM-25 and T-BCM-25 ($p = 0.047$, t test), as well as among NT-BCM-25, NT-BCM-60, and T-BCM-60 ($p < 0.039$, ANOVA).

It should be noted that some of the FITC-stained regions were devoid of BCMs; these vessels could represent nonfunctional vessels that are disconnected from the tumor vasculature network. CD31 is a cluster of molecules that are expressed on several types of cells including platelets, macrophages, and endothelial cells.[29] Therefore, recognition of CD31 molecules by the anti-CD-31-antibody may also occur on endothelial cells that are distant from functional blood vessels.

In Vivo **Internalization and Subcellular Distribution of BCMs.** Figures 5a and 5b illustrate the *in vivo* subcellular distribution of BCMs in MDA-MB-468 and MCF-7 tumor-bearing mice, respectively, at 48 hpi. For MDA-MB-468 tumor-bearing mice, the amounts of T-BCMs in the extracellular compartments (membrane bound + interstitial accumulation) were found to be higher, compared to NT-BCMs for both particle sizes ($p < 0.029$). A significant enhancement in cytoplasmic uptake due to molecular

(29) Jackson, D. E. The unfolding tale of PECAM-1. *FEBS Lett.* **2003**, *540*, 7–14.

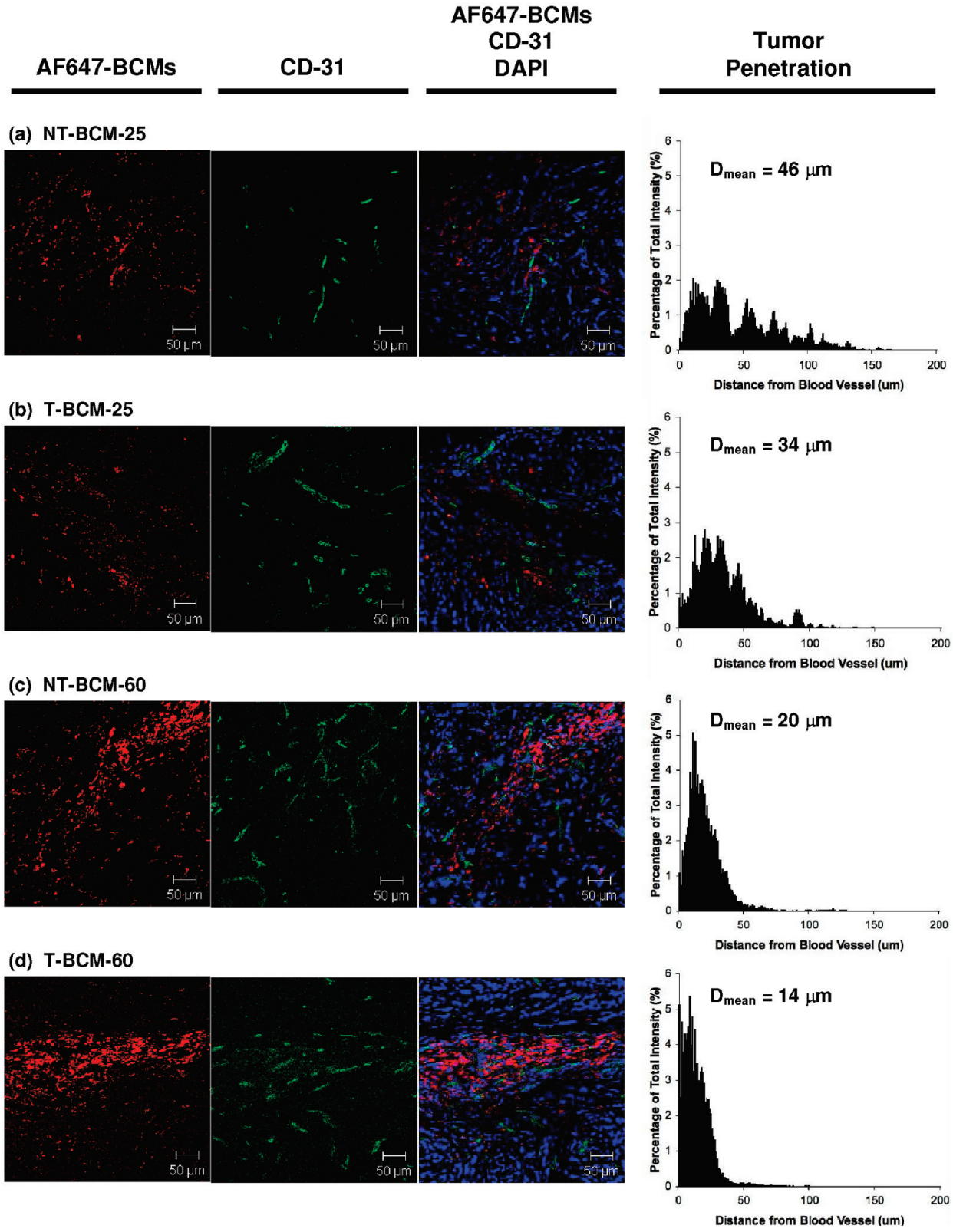

Figure 4. Tumor penetration of AF647-labeled (a) NT-BCM-25, (b) T-BCM-25, (c) NT-BCM-60, and (d) T-BCM-60 in MDA-MB-468 tumors captured by fluorescence confocal microscopy. MDA-MB-468 tumor-bearing mice were injected with AF647-labeled BCMs (red signal) and were sacrificed at 48 hpi. 8 μm thick tumor sections were stained with FITC-anti-CD-31-antibody (green signal) and DAPI (blue signal) for visualization of tumor blood vessels and cell nuclei, respectively. Overlay images that include all three signals were also included as the third panel of images from the left. The distances between each red pixel (BCMs) and the nearest green pixel (blood vessels) in each image were calculated using a customized algorithm in MATLAB, and are shown in histograms presented in the right panel.

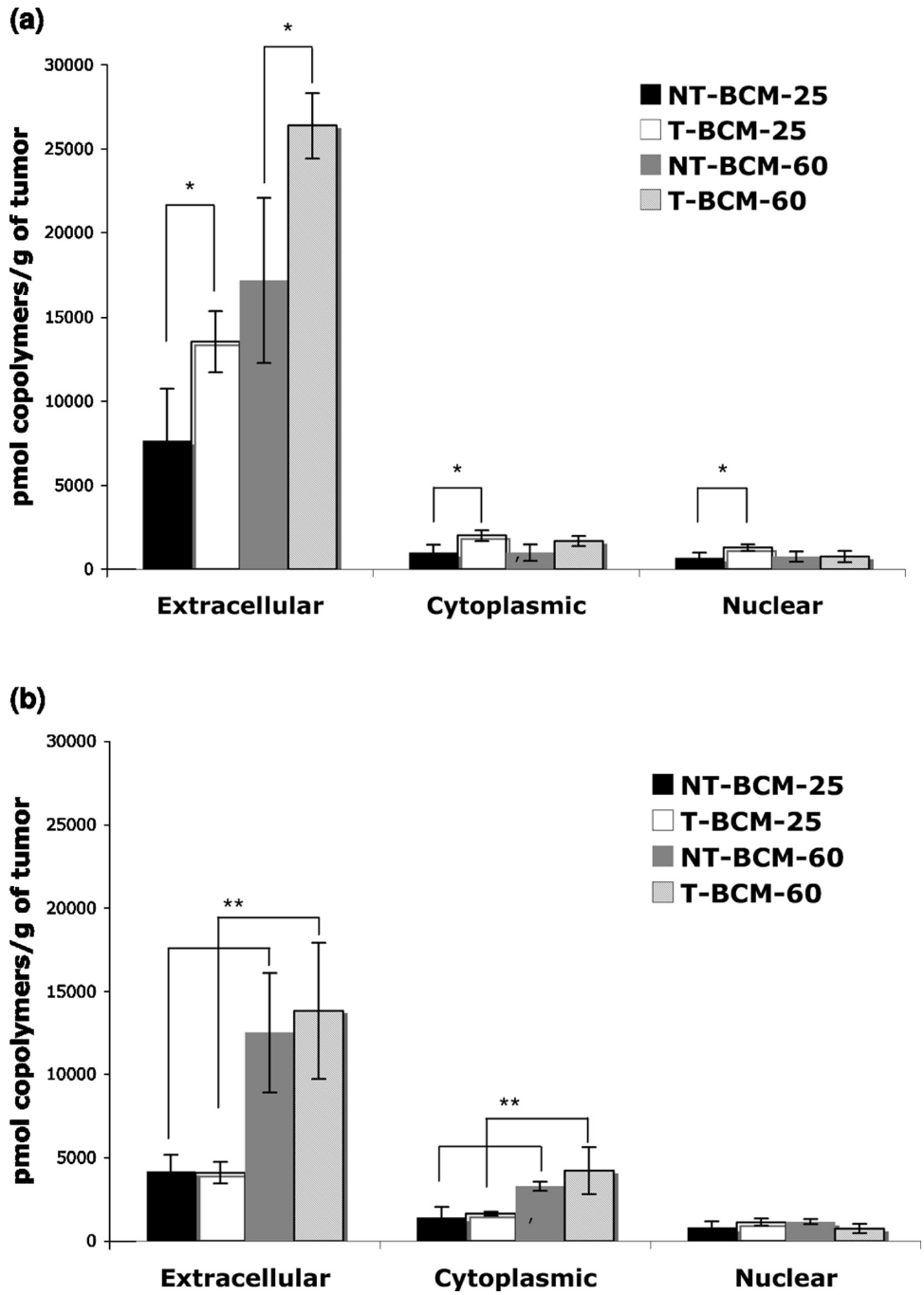

Figure 5. *In vivo* subcellular distribution of ^{111}In-BCM-25 and ^{111}In-BCM-60 in (a) MDA-MB-468 and (b) MCF-7 tumors. Tumors were harvested at 48 hpi, fractionated into extracellular, cytoplasmic, and nuclear fractions. γ-Counting was performed for quantification of ^{111}In-labeled BCMs in each subcellular fraction ($n \geq 3$, error bars represent SD). *$p <$ 0.029 for comparison between NT-BCMs and T-BCMs as determined by independent *t* test. **$p <$ 0.034 for comparison between BCM-25 and BCM-60 as determined by independent *t* test.

targeting was only detected for BCM-25 ($p = 0.018$), and was statistically insignificant for BCM-60 ($p = 0.104$). A significant increase in the nuclear uptake of BCMs was only observed in the MDA-MB-468 tumor-bearing mice injected with T-BCM-25 ($p = 0.032$). Molecular targeting did not induce any changes in the subcellular distribution of BCMs in the MCF-7 tumors ($p > 0.9$). The *in vivo* cytoplasmic uptake and extracellular accumulation of BCMs in the MCF-7 tumors were found to be size-dependent. In general, BCM-60 was delivered to the MCF-7 tumors (intracellular and extracellular) more efficiently than BCM-25 ($p > 0.9$).

In Vitro **Internalization and Subcellular Distribution of BCMs.** Figures 6a and 6b present the *in vitro* subcellular distribution of BCMs following a 24 h incubation period with MDA-MB-468 and MCF-7 cells, respectively. It was found that the *in vitro* cytoplasmic uptake of BCM-60 was

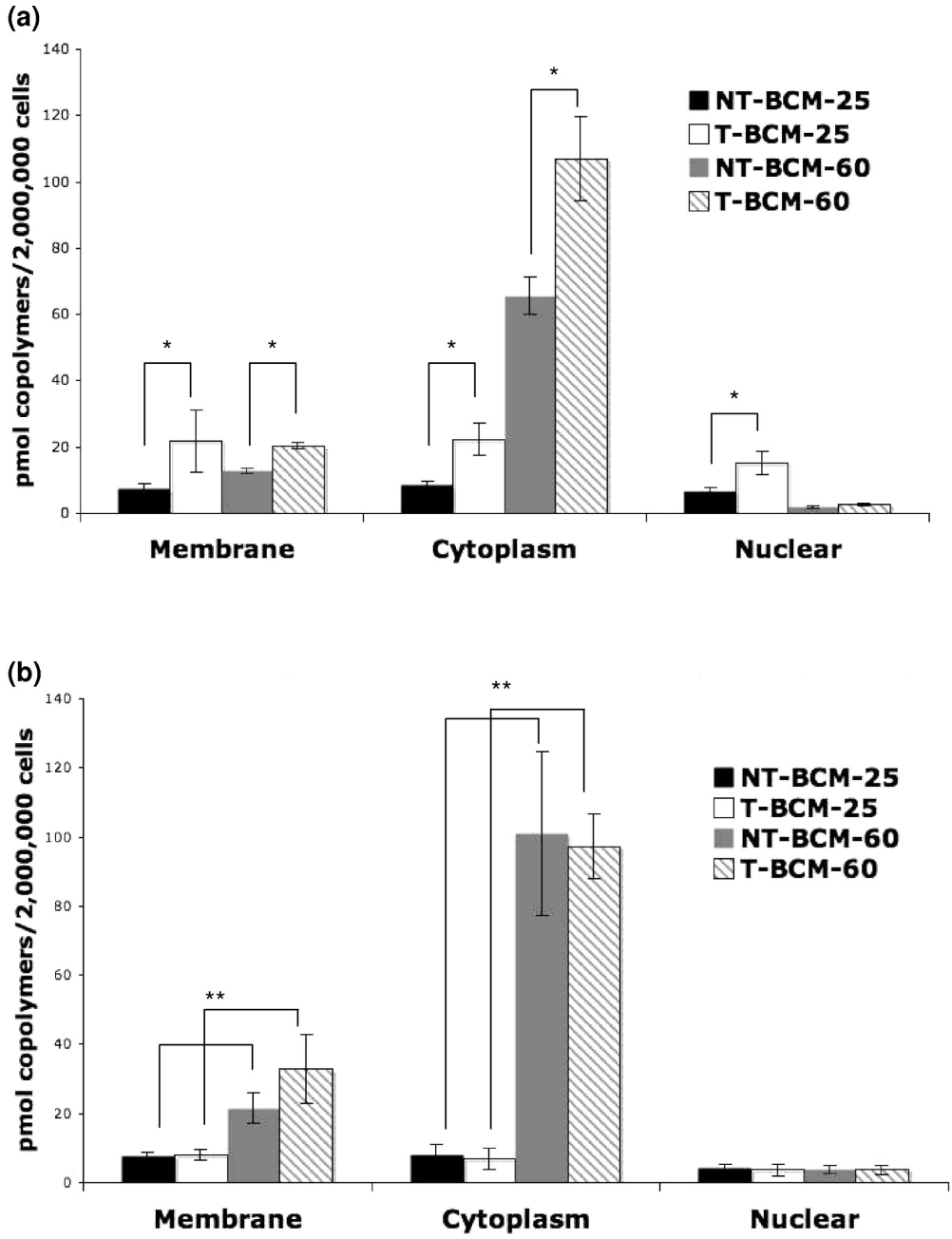

Figure 6. *In vitro* subcellular distribution of ^{111}In-BCM-25 and ^{111}In-BCM-60 in (a) MDA-MB-468 and (b) MCF-7 breast cancer cells. Breast cancer cells were incubated with the above treatments for 24 h prior to subcellular fractionation. γ-Counting was performed for quantification of ^{111}In-BCMs in each subcellular fraction ($n \geq 3$, error bars represent SD). *$p < 0.027$ for comparison between NT-BCMs and T-BCMs as determined by independent *t* test. **$p < 0.045$ for comparison between BCM-25 and BCM-60 as determined by independent *t* test.

significantly greater than BCM-25 in both cell lines ($p < 0.001$). Also, a greater amount of NT-BCM-60 was found to be associated with the cell membrane in comparison to NT-BCM-25 ($p = 0.014$ for MDA-MB-468 and $p = 0.003$ for MCF-7), indicating that the increased NT-BCM cytoplasmic uptake is a result of enhanced nonspecific binding and subsequent fluid phase endocytosis.[30] In addition, increased uptake of T-BCM-60 in MDA-MB-468 cells is likely a combined result of enhanced specific and nonspecific interactions between the T-BCMs and the EGFR-overexpressing cells. This is supported by the fact that there was no significant difference between the levels of cytoplasmic or cell membrane bound BCMs in the low EGFR-expressing MCF-7 cells following incubation with NT-BCMs or T-BCMs ($p > 0.611$).

In vitro nuclear uptake of BCMs was found to be dependent on particle size and molecular targeting. While both NT-BCM-25 and T-BCM-25 exhibit higher than base-

(30) Amiji, M. M. *Nanotechnology for cancer therapy*; CRC/Taylor & Francis: Boca Raton, 2007; p 817, [8] of plates.

line levels of nuclear accumulation (compared to ^{111}In-DTPA, negative control) ($p < 0.036$) in the MDA-MB-468 cells, the nuclear uptake of T-BCM-25 was found to be 2-fold higher than NT-BCM-25 ($p = 0.011$). In addition, the amount of BCM-60 (NT-BCMs and T-BCMs) accumulated within the nuclei was similar to baseline levels ($p > 0.05$). No significant increase in the nuclear uptake of any of the ^{111}In-labeled constructs studied was observed in the MCF-7 cells ($p > 0.14$).

Discussion

The current study demonstrates that manipulation of BCM particle size and molecular targeting leads to distinct whole body, intratumoral, and subcellular BCM distribution profiles in human breast cancer xenografts expressing differential levels of EGFR. NT-BCM-25 was shown to have faster plasma clearance and lower tumor deposition than NT-BCM-60. The accelerated plasma clearance of BCM-25 is not attributed to micelle dissociation as BCM-25 and BCM-60 have similar thermodynamic stability. Furthermore, the plasma concentrations of BCM-25 and BCM-60 immediately following administration were approximately 100-fold above their CMC values. Therefore, the early onset of BCM-25 clearance, which clearly deviates from the clearance rate of BCM-60 in Figure 1, supports that BCM-25 was cleared as intact nanoparticles during the distribution phase. However, it should be noted that as the plasma copolymer concentration falls below the CMC (e.g., at the elimination phase), the rate of BCM dissociation depends on the kinetic stability of the BCM systems. Because BCM-25 is composed of copolymers with a shorter hydrophobic block than BCM-60, BCM-25 may become more susceptible to dissociation at concentrations below the CMC over an extended period of time. Nevertheless, it has been reported that other nondissociable nanoparticles of similar particle size also exhibit accelerated plasma clearance and broader tissue distribution compared to their larger counterparts.[31,32] Pharmacokinetics analyses revealed that NT-BCM-25 was eliminated ($k_{10} = 0.36 \pm 0.02$/h) significantly faster than NT-BCM-60 ($k_{10} = 0.031 \pm 0.004$/h) from the central compartment (i.e., highly perfused tissues such as plasma, kidneys, spleen, liver). However, elimination of BCM-25 from the circulation through glomerular or splenic filtration is unlikely as the kidneys and the spleen are known to predominantly filter particles of <5.5 nm and >200 nm, respectively.[15] The livers of mice consist of endothelial fenestrations that range from 50 to 1000 nm (with ~70% of fenestrae <100 nm) in diameter and therefore allow for efficient elimination of BCM-25 from the circulation, followed by clearance via hepatobiliary excretion.[33] Although the liver uptake of BCM-25 was found to be similar to that of BCM-60 at 48 hpi, it has been reported that hepatobiliary transfer of polymeric macromolecules is extremely effective and the amount accumulated in the liver is significantly reduced beyond 24 hpi.[34,35]

In general, NDDS with short circulation half-lives often have low total tumor deposition, as an extended plasma residence time is a prerequisite for efficient exploitation of the EPR effect.[22,36] The low concentration of BCM-25 in the circulation postinjection greatly reduces the gradient for their tranvascular transport into the interstitial space. Outward convective flow caused by elevated interstitial fluid pressure (IFP) may also lead to clearance of the extravasated BCM back into the circulation. It is postulated that the vascular permeability of BCM-25 was higher than BCM-60 due to the smaller particle size, and hence BCM-25 undergoes a faster clearance from the tumor.[16,37] A similar observation was noted for immunoglobulin G (IgG) fragments (i.e., Fab′ and scFv) which were found to be associated with a more rapid tumoral clearance than the larger intact IgG.[18] Nonspecific binding of BCM-60 to cells or extracellular matrix (ECM) components also enhances their retention within the tumor compared to BCM-25 (BCM-25 has lower nonspecific binding affinity toward both MDA-MB-468 and MCF-7 cells as shown in Figure 6). Similarly, the ligand−receptor interaction between the T-BCM (EGF+) and EGFR overexpressed on the MDA-MB-468 cells also delays T-BCM tumoral clearance.[19] For instance, the MDA-MB-468 tumor uptake of T-BCM-25 was shown to be comparable to NT-BCM-60, even though the circulation half-life of T-BCM-25 was significantly shorter. This retention effect is also evident in the autoradiography study where tumor regions with similar blood vessel densities were able to retain a higher level of T-BCM-25 (Figure 3b) than NT-BCM-25 (Figure 3a) at 48 hpi. These results support that BCM extravasation and tumor vascularization are not the sole determinants of total tumor deposition of BCMs.

Although autoradiography failed to detect any differences in the tumor penetration of the four treatment groups,

(31) Sonavane, G.; Tomoda, K.; Makino, K. Biodistribution of colloidal gold nanoparticles after intravenous administration: effect of particle size. *Colloids Surf., B* **2008**, *66*, 274–80.

(32) Yang, Z.; Leon, J.; Martin, M.; Harder, J. W.; Zhang, R.; Liang, D.; Lu, W.; Tian, M.; Gelovani, J. G.; Qiao, A.; Li, C. Pharmacokinetics and biodistribution of near-infrared fluorescence polymeric nanoparticles. *Nanotechnology* **2009**, *20*, 165101.

(33) Igarashi, E. Factors affecting toxicity and efficacy of polymeric nanomedicines. *Toxicol. Appl. Pharmacol.* **2008**, *229*, 121–34.

(34) Cartlidge, S. A.; Duncan, R.; Lloyd, J. B.; Kopeckova-Rejmanova, P.; Kopecek, J. Soluble, crosslinked N-(2-hydroxypropyl)methacrylamide copolymers as potential drug carriers: 3. Targeting by incorporation of galactosamine residues. Effect of route of administration. *J. Controlled Release* **1987**, *4*, 265–78.

(35) Noguchi, Y.; Wu, J.; Duncan, R.; Strohalm, J.; Ulbrich, K.; Akaike, T.; Maeda, H. Early phase tumor accumulation of macromolecules: a great difference in clearance rate between tumor and normal tissues. *Jpn J. Cancer Res.* **1998**, *89*, 307–14.

(36) Moghimi, S. M.; Hunter, A. C.; Murray, J. C. Long-circulating and target-specific nanoparticles: Theory to practice. *Pharmacol. Rev.* **2001**, *53*, 283–318.

(37) Yuan, F.; Dellian, M.; Fukumura, D.; Leunig, M.; Berk, D. A.; Torchilin, V. P.; Jain, R. K. Vascular permeability in a human tumor xenograft: molecular size dependence and cutoff size. *Cancer Res.* **1995**, *55*, 3752–6.

examination using confocal fluorescence microscopy revealed that particle size and molecular targeting affect the BCM intratumoral transport at the micrometer scale. In solid tumors, penetration of extravasated macromolecules from the perivascular region into the avascular region is in part governed by diffusion, where their diffusivity is inversely correlated with their molecular size.[17,18,38] The tortuosity of the ECM and the high cellular density in the tumor pose significant barriers to diffusion of large molecules.[39] Several groups have studied the *in vitro* tumor penetration of polymeric nanoparticles using multicellular spheroids; few have extended their studies into *in vivo* tumor-bearing models.[3,40] In the current study, BCM-25 was found to diffuse further away from the tumor blood vessels than BCM-60, using both qualitative and quantitative means (Figure 4). Similar to observations regarding tumor penetration of scFv and IgG, the smaller BCM-25 were found to have a more homogeneous intratumoral distribution than the larger BCM-60, which mainly localized in the perivascular region.[17,18] Interestingly, the mean diffusion distance (D_{mean}) of T-BCM-25 from the nearest blood vessels was found to be statistically lower than NT-BCM-25 in the MDA-MB-468 tumors. This is likely attributed to the phenomenon known as "binding site barrier" which can occur as a result of molecular targeting.

The concept of binding site barrier was first introduced and proven experimentally by Weinstein and colleagues, where specific binding and/or cellular internalization of antibodies by the targeted cells halts their penetration in solid tumors.[41] For instance, mathematical modeling indicates that it should only take 15 min for an antibody to diffuse 100 μm via simple Brownian motion; however, similar diffusion may require hours if filling of antibody binding sites is taken into account, without considering systemic and endocytic clearance within the tumors.[17] Goodman et al. demonstrated *in silico* that 40 nm nanoparticles with an overestimated binding affinity toward cells in multicellular spheroids undergo no penetration, possibly attributed to the binding site barrier effect.[39] To the best of our knowledge, the current study is one of the first to report that molecular targeting can lead to binding site barrier for polymer nanoparticle delivery systems *in vivo*. It should be noted that the binding site barrier effect was only observed with the BCM-25 but not BCM-60. This could be attributed to the differences in their rates of tumor penetration and binding/internalization, as the materialization of the binding site barrier effect depends on the balance between these two factors.[17,42]

The presence of binding site barrier and limited tumor penetration of BCMs severely hampered BCM−cell interactions within the tumors. *In vitro*, monolayer grown cancer cells were homogeneously saturated with BCMs present within the incubation media, whereas *in vivo* only a small percentage of the tumor cells were exposed to the extravasated BCMs. Because of this, the effect of particle size and molecular targeting on the cellular uptake and subcellular distribution of BCMs became much less pronounced *in vivo* (Figures 5 and 6).

Understanding the subcellular distribution of NDDS has far-reaching implications on their use in particular therapeutic applications. It is believed that direct delivery of the therapeutic content of NDDS to their subcellular targets can lead to significant therapeutic advantage. In our previous study, we demonstrated that T-BCM (EGF+) localize mainly in the perinuclear region with a minority of T-BCM localizing in the cell nuclei of MDA-MB-468 cells.[10] This is attributed to the intrinsic nuclear translocation properties of EGF upon binding to cell surface EGFR,[20,21] which has also been observed in MDA-MB-468 cells incubated with ^{111}In-labeled EGF ($p < 0.05$ compared to free ^{111}In-DTPA baseline, data not shown). A significant increase in the amount of T-BCM-25 was detected in the cell nuclei of MDA-MB-468 cells compared to NT-BCM-25, both *in vitro* and *in vivo*. It should be noted that nuclear transport of T-BCM-25 was only observed in the MDA-MB-468 cells but not in the MCF-7 cells, which express 100-fold less EGFR/cell. Targeting motifs that are less specific such as the TAT peptide, which consist of both cell penetrating and nuclear-localizing sequences, can be utilized for promoting cellular uptake and nuclear translocation of NDDS into a wide variety of cell types.[43] Aside from the choice of targeting motif, particle size is also an important factor to be considered when designing NDDS for nuclear delivery. In the current study, the nuclear uptake of BCM-60 (NT- and T-BCM) was found to be similar to the baseline level, as only particles with diameters of less than 39 nm have be en reported to be actively transported into cell nuclei through the nuclear pore complex.[44] This observation also agrees with the literature wherein many NDDS, including liposomes

(38) Pluen, A.; Boucher, Y.; Ramanujan, S.; McKee, T. D.; Gohongi, T.; di Tomaso, E.; Brown, E. B.; Izumi, Y.; Campbell, R. B.; Berk, D. A.; Jain, R. K. Role of tumor-host interactions in interstitial diffusion of macromolecules: cranial vs. subcutaneous tumors. *Proc. Natl. Acad. Sci. U.S.A.* **2001**, *98*, 4628–33.

(39) Goodman, T. T.; Chen, J.; Matveev, K.; Pun, S. H. Spatio-temporal modeling of nanoparticle delivery to multicellular tumor spheroids. *Biotechnol. Bioeng.* **2008**, *101*, 388–99.

(40) Goodman, T. T.; Olive, P. L.; Pun, S. H. Increased nanoparticle penetration in collagenase-treated multicellular spheroids. *Int. J. Nanomed.* **2007**, *2*, 265–74.

(41) Juweid, M.; Neumann, R.; Paik, C.; Perez-Bacete, M. J.; Sato, J.; van Osdol, W.; Weinstein, J. N. Micropharmacology of monoclonal antibodies in solid tumors: direct experimental evidence for a binding site barrier. *Cancer Res.* **1992**, *52*, 5144–53.

(42) Thurber, G. M.; Schmidt, M. M.; Wittrup, K. D. Factors determining antibody distribution in tumors. *Trends Pharmacol. Sci.* **2008**, *29*, 57–61.

(43) Costantini, D. L.; Hu, M.; Reilly, R. M. Peptide motifs for insertion of radiolabeled biomolecules into cells and routing to the nucleus for cancer imaging or radiotherapeutic applications. *Cancer Biother. Radiopharm.* **2008**, *23*, 3–24.

(44) Pante, N.; Kann, M. Nuclear pore complex is able to transport macromolecules with diameters of about 39 nm. *Mol. Biol. Cell* **2002**, *13*, 425–34.

(greater than 80 nm in diameter), fail to accumulate in the cell nucleus.[13,45]

The findings from the current study provide key information on the design parameters of NDDS that can give rise to differences in the whole body, intratumoral, and cellular transport of these particles *in vivo*. The results presented here represent the *in vivo* fate of nonionic polymeric nanoparticles with hydrodynamic diameters of approximately 25 and 60 nm. Future studies may focus on other NDDS with different properties, or include monitoring of the *in vivo* distribution of encapsulated therapeutic agents. It would also be of interest to investigate the NDDS tumor penetration kinetics by performing similar studies over an extended period of time. Several studies have suggested that peak tumor penetration differs for particles with different molecular sizes, and that larger molecules can indeed achieve similar tumor penetration as smaller molecules over an extended time frame.[18] In addition, tumor penetration of molecules also depends on the biological properties of the implanted tumors and the animal models employed. ECM composition and structure, which can vary greatly depending on the types and sites of the tumors or the host origin, are extremely influential in determining the intratumoral transport of molecules.[38,39] These factors pose a significant challenge to thoroughly understanding the *in vivo* transport behavior of NDDS in solid tumors. While intratumoral transport of drug molecules and antibodies has been studied extensively,[17,46] evaluation of the tumor penetration of NDDS represents an underdeveloped area of research.

(45) Shuai, X.; Ai, H.; Nasongkla, N.; Kim, S.; Gao, J. Micellar carriers based on block copolymers of poly(epsilon-caprolactone) and poly(ethylene glycol) for doxorubicin delivery. *J. Controlled Release* **2004**, *98*, 415–26.

(46) Minchinton, A. I.; Tannock, I. F. Drug penetration in solid tumours. *Nat. Rev.* **2006**, *6*, 583–92.

Conclusions

The integration of interdisciplinary techniques has unveiled important information on the *in vivo* tumor penetration and subcellular distribution of NDDS. While the preparation and *in vitro* characterization of novel T-NDDS are commonly reported, thorough *in vivo* characterization detailing their ability to overcome biological barriers is often lacking. The current study demonstrated that BCMs with a short circulation half-life could achieve comparable tumor deposition to that of BCMs with an extended plasma residence time, by delaying their tumoral clearance via molecular targeting. On the other hand, reducing particle size promotes BCM penetration into solid tumors, but functionalizing the particle surface with a targeting moiety retards their tumor penetration due to the binding site barrier effect. Therefore, it is crucial to carefully balance the different NDDS design parameters in order to truly optimize their *in vivo* performance for specific therapeutic applications.

Acknowledgment. This study is supported by funding from Canadian Institutes of Health Research, Canadian Breast Cancer Research Alliance, and Ontario Institute for Cancer Research, awarded to C.A. and R.M.R. The authors are grateful to the Natural Sciences and Engineering Research Council of Canada, Hoffman-La Roche/Rosemarie Hager, and Lorne F. Lambier for scholarships awarded to H.L., as well as the MDS-Nordion Graduate Scholarship in Radiopharmaceutical Sciences awarded to B.H. The authors thank Deborah Scollard and Joanne Leung for technical assistance with the animal studies and the MATLAB algorithm for the confocal fluorescence microscopy studies, respectively. The authors also thank Anton Semechko from Dr. David A. Jaffray's Laboratory and STTARR core IV for technical support on the MATLAB algorithm for the autoradiography studies.

MP100038H